

CrystEngComm

Accepted Manuscript



This is an *Accepted Manuscript*, which has been through the Royal Society of Chemistry peer review process and has been accepted for publication.

Accepted Manuscripts are published online shortly after acceptance, before technical editing, formatting and proof reading. Using this free service, authors can make their results available to the community, in citable form, before we publish the edited article. We will replace this *Accepted Manuscript* with the edited and formatted *Advance Article* as soon as it is available.

You can find more information about *Accepted Manuscripts* in the [Information for Authors](#).

Please note that technical editing may introduce minor changes to the text and/or graphics, which may alter content. The journal's standard [Terms & Conditions](#) and the [Ethical guidelines](#) still apply. In no event shall the Royal Society of Chemistry be held responsible for any errors or omissions in this *Accepted Manuscript* or any consequences arising from the use of any information it contains.

Crystallization Mechanism Analysis of Noncrystalline Ni-P Nanoparticles through XRD, HRTEM and XAFS

**Yuanyuan Tan¹, Dongbai Sun¹, Hongying Yu^{3, *}, Bin Yang¹, Yu Gong², Shi Yan¹,
Zhongjun Chen², Quan Cai², Zhonghua Wu^{2, *}**

1: National Center for Materials Service Safety, University of Science and Technology

Beijing, Beijing 100083, PR China

2: Institute of High Energy Physics, Chinese Academy of Sciences, & Graduate University of

Chinese Academy of Sciences, Beijing 100049, PR China

3: Corrosion and Protection Center, Laboratory for Corrosion-Erosion and Surface

Technology, University of Science and Technology Beijing, Beijing 100083, PR China

***: Correspondence to: Zhonghua WU, E-mail: wuzh@ihep.ac.cn**

Hongying Yu, E-mail: hyyu@ustb.edu.cn

Abstract

The crystallization behavior of noncrystalline Ni-P nanoparticles prepared by liquid-phase pulsed-discharge was studied through XRD, HRTEM, X-ray Absorption Fine Structure spectra (XAFS) from both Ni K-edge and P K-edge. The growth of crystalline Ni₃P and Ni are completing. The main phases within the particles are crystalline Ni₃P and Ni, while the metastable phases Ni₅(P, Ni)₂ presented as coated shell in the outside of the particles. The appearance of feature D in P K-edge XANES spectrum could be used as a characteristic for the formation of long-range ordered Ni₃P. The standard deviation ($\Delta R/R$) of the fitting P-Ni bondlength from the theoretical value of Ni₃P crystal could be used to define the crystallization process. Although the nanoparticles were observed as XRD-amorphous at 250 °C, their magnetic property can be attributed to the formation of FCC-Ni clusters. A crystallization mechanism has been proposed to describe the crystallization process of the as-prepared noncrystalline Ni-P nanoparticles.

Key words: Noncrystalline Ni-P nanoparticles; XRD; HRTEM; XAFS; Crystallization mechanism.

1. Introduction

Crystallization behavior of amorphous Ni-P system has been extensively studied since 1980s, especially the as-deposited Ni-P alloys. However, these works were mostly based on X-ray diffraction (XRD) patterns and high resolution transmission electron microscopy (HRTEM) pictures, which were used to extract structure and phase changes from diffraction peaks and electron diffraction patterns. It is known that XRD peaks and electron diffraction patterns are powerful to study crystalline structures. However, X-ray and electron diffraction techniques could not detect the structure changes when the sample is XRD amorphous. Therefore, the changes of short-range ordered structures during crystallization process were scarcely reported due to the technical limitation of XRD and HRTEM.

The structure of Ni-P alloys has been reported to be dependent on their phosphorus content [1-3]. In general, the as-deposited Ni-P alloys can be classified as low-P, medium-P and high-P Ni-P types based on their phosphorus contents. The low-P alloys are presented as microcrystalline nickel [2] or crystalline phase [3]. The medium-P and high-P alloys can be either amorphism [4] or mixtures of amorphous and microcrystalline phases like Ni_5P_2 , Ni_3P_4 and Ni_{12}P_5 [5-9]. Most investigators agreed on that the amorphous Ni-P systems become crystallized when they were heated and then different phases would appear, despite of the differences of opinions on concerning their initial structures. Since the solid solubility limit of phosphorus in crystalline nickel is very low, the Ni-P alloys are generally in metastable states, and their stability depends strongly on the composition. Therefore, the crystalline procedure can be very different due to the variations of alloy composition. For example, amorphous Ni-P nanospheres with a low-P content were directly crystallized into Ni_3P and FCC-structure Ni [10, 11]. However, for the specimens with high-P contents, the sequence of phase transformation of Ni-P system was from initial amorphous phase, to intermediate mixed phases consisted of unknown metastable phases and stable Ni_3P phase (+ FCC Ni), then to final stable Ni_3P phase (+FCC Ni) [10-12].

These reported crystallization mechanisms and intermediate phases involved in amorphous Ni-P alloys were mainly based on the XRD patterns, TEM/HRTEM micrographs and differential scanning calorimetric (DSC) studies. However, these experimental methods could hardly provide effective information until the test specimen becomes long-range ordered. The atomic-level microstructure changes in the initial crystallization process therefore could not be detected, which can be attributed to the insensitivity to such a structure and/or the resolution limitations of XRD, TEM and DSC techniques. Fortunately, X-ray absorption near-edge structure (XANES) is sensitive to the electronic and geometric structures, and extended X-ray absorption fine structure (EXAFS) can be used to resolve the local atomic structure. Therefore, X-ray absorption fine structure (XAFS) spectroscopy is a unique tool to study the atomic-level structure around the selected elements [13]. XAFS technique has been successfully used to resolve the local structures in colloidal nanocrystals [14-17]. Both structures of XRD-amorphous and XRD-crystalline materials can be determined in fine detail [18]. Consequently, XAFS could be powerful to monitor the initial crystallization behavior of amorphous Ni-P nanoparticles by probing the atomic-level structure change.

This study was undertaken to study initial crystallization behavior of amorphous Ni-P nanoparticles produced by liquid-phase pulsed-discharge method. In combination XAFS with XRD, HRTEM and vibrating sample magnetometer (VSM), the structure changes both in short-range and long-range order of Ni-P nanoparticles during the heating process will be studied complementally. XRD give crystalline phases and phase changes. HRTEM provides direct insight into morphology and size-distribution. XAFS probes the changes of local atomic structure and chemical valence especially for XRD- amorphous samples. VSM enables the study of magnetic properties corresponding to different crystallization stages. Hence, a complete picture of the crystallization behavior of amorphous Ni-P nanoparticles and its structural properties can be obtained through cooperative use of these methods.

2. Experiments

The amorphous Ni-P nanoparticles were prepared by using the liquid pulsed-discharge method [19]. 78.15 at% of Ni and 21.85 at% of P constituted the as-prepared Ni-P nanoparticles from the composition analysis of Inductively Coupled Plasma-Mass Spectroscopy (ICP-MS). Heat treatments of the as-prepared specimens were carried out under argon atmosphere in a tube furnace. The as-prepared Ni-P nanoparticles were divided into several pieces. One was kept at room temperature without heat treatment. The others were individually heated to the target temperatures 200, 250, 300, 350, 400, 450, 500, 550, 650, 700, and 750°C with a heating rate of 10 °C/min. The holding time at each target temperature for every sample is 2h. Afterwards, the sample was cooled to room temperature naturally under the same argon atmosphere. Finally, the sample was ground with agate mortar and pestle for several minutes to make it suitable for the following tests.

HRTEM samples were prepared by re-dissolving the annealed specimens into ethanol, forming respective suspensions. Then one drop of each suspensions was dropped onto the ultra-thin carbon-coated copper grid to form the TEM samples after the ethanol evaporation. TEM observations were taken on the JEOL JEM-2010 electron microscope operated at 200 KV with a beam current of 105 μ A. Room-temperature XRD patterns of these annealing samples were collected at the beamline 4B9A in Beijing Synchrotron Radiation Facility (BSRF).

Ni K-edge XAFS measurements in transmission mode were performed at beamline 4B9A of BSRF. The storage ring was operated at 2.5 GeV with the maximum current of 250 mA. The incident X-ray was monochromatized by using a double-crystal Si (111) monochromator to choose the monochromatic X-ray energy from 8133 to 9133 eV with an energy resolution ($\Delta E/E$) of about 2×10^{-4} . Both the incident and transmission X-ray intensities were collected with ion chambers. P K-edge XAFS data were collected in fluorescence mode at Beamline 4B7A of BSRF. The incident X-ray energy was chosen by a double-crystal Si (111) monochromator with a scanning energy range from 2100 to 2754 eV. The Ni-P powder samples were

smearred on a carbon adhesive tape, which was mounted into a vacuum chamber for the XAFS measurements. The fluorescence signal was collected with a Si (Li) detector. These XAFS data of Ni and P K-edge were analyzed by using the Demeter software package (Univ. of Chicago) [20]. The reference spectra of Ni and P K-edges were calculated by using FEFF9 code (Univ. of Washington) [21]. Specific structural information, such as coordination number, interatomic spacing and mean-squared disorder [22], could be determined through fitting well-matched theoretical pathways to the experimental spectra..

3. Results and Discussion

3.1 XRD patterns and HRTEM images

XRD patterns of all these specimens are shown in Fig. 1. It can be seen that only one broad peak centered at 2θ of about 44.5° appeared on the XRD patterns until the heating temperature reached to 300°C . This suggests that the Ni-P nanoparticles are in noncrystalline structure as the heating temperature is below 300°C . Therefore, the structure and phase of Ni-P nanoparticles were assumed to be invariable during these process if we only have XRD patterns. After the specimen was heated to 300°C for two hours, diffraction peaks attributed to Ni_3P (according to the JPCD 34-0501) and a metastable phase $\text{Ni}_5(\text{P}, \text{Ni})_2$ [10, 12, 23] appeared simultaneously. While the peaks from FCC Ni (according to the JPCD 04-0850) at 44.5° and 51.8° could not be clearly identified. These peaks at 41.8° , 43.6° , 45.2° , 46.6° , 50.6° and 52.7° can be indexed as the (231), (112), (240), (141), (222), and (132) reflections of crystalline Ni_3P , respectively. With the heating temperature raising to 350°C , the diffraction peaks of Ni_3P became sharp, and some weak diffraction peaks of Ni_3P also appeared on the region from 55° to 100° . The peaks from FCC Ni were also visible, indicating the formation of long-range ordered Ni. The metastable phase with peaks at 37.6° , 47.3° and 48.2° was also intensified. With the heating temperature raising from 400 to 650°C , the peaks from Ni_3P grew up continuously, but their intensities increased very slowly as compared to these from FCC Ni. Especially, the (111) peak at 44.5° of the

FCC Ni ascended rapidly from hardly to be seen to a height nearly the same with the (231) peak at 41.8° of Ni_3P . While the (200) peak at 51.7° of FCC Ni, which could not be separated from the peak at 51.9° of Ni_3P at 400°C , was almost two times the height of the peak of 51.9° at 650°C . The other three peaks at 76.4° , 92.9° and 98.5° indexed as the (220), (311), and (222) reflections of FCC Ni were also raised up quickly at the same time. However, the peaks from metastable phase $\text{Ni}_5(\text{P}, \text{Ni})_2$ were changed little in this heating temperature range. After the specimens were further heated to 700 and 750°C , the peaks from $\text{Ni}_5(\text{P}, \text{Ni})_2$ disappeared, leaving only the peaks from Ni_3P and Ni. This change demonstrates that the final stable phases are Ni_3P and FCC Ni during the crystallization process of amorphous Ni-P nanoparticles.

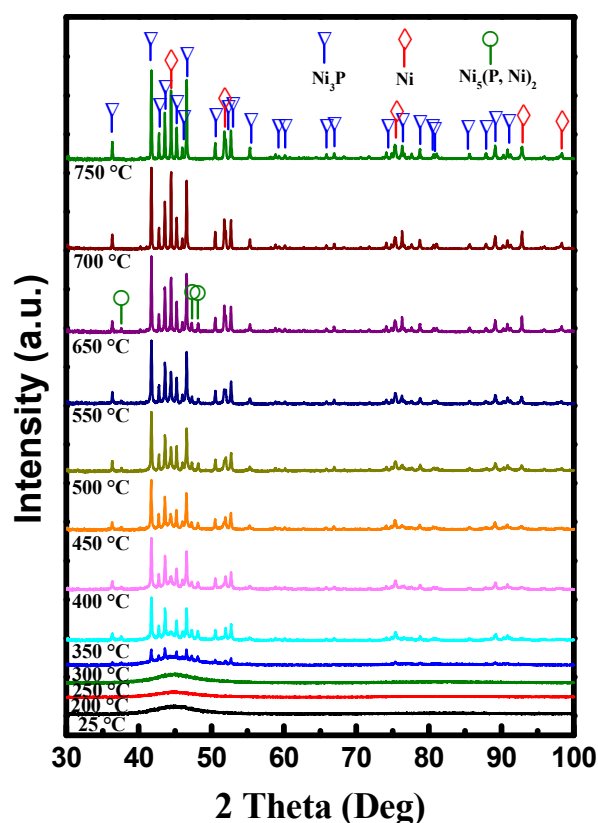


Figure 1. XRD patterns of Ni-P samples after heat-treatment at different temperatures.

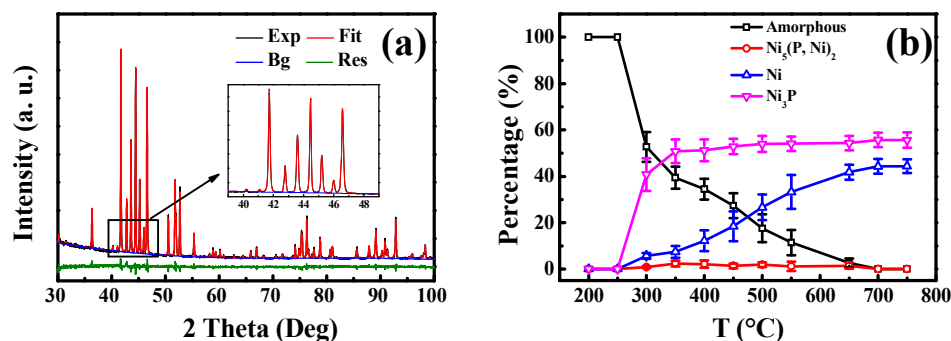


Figure 2. (a) Typical refinement result of the XRD pattern for the Ni-P nanoparticles annealed at 700°C. The peaks ranging from 40 to 50° were enlarged in the inset for clarity. (b) Changes of phase contents with the heat-treatment temperature. These phase contents were obtained from the refinements of XRD patterns.

The change of diffraction intensities for the different crystalline phases indicates that the phase contents are changeable with the heat-treatment temperature. In order to get the phase contents, the Rietveld method [24, 25] was used to refine the diffraction patterns by using the Maud program. During the refinement, the background was fitted by the Chebyshev polynomial function implemented in the program. The peak profiles were modeled by a modified pseudo-Voigt profile function. Reference structures (CIF files) of Ni₃P (JPCD 34-0501), Ni (JPCD 04-0850) and Ni₅P₂ (JPCD 17-0225) were used as standard phase files. Refinements were carried out until convergence was reached and the Rwp factor reached to about 10%. As an example, the fitting results for the sample annealed at 700 °C is shown in Fig. 2(a). Based on the refinements, the changes of phase contents were calculated as shown in Fig. 2(b).

From Fig. 2, it can be seen that the sample contains only an amorphous phase when the heating temperature was below 250 °C. With the heating temperature increasing above 250°C, the phase contents in the specimens had different variations. The phase content of crystalline Ni₃P increased sharply from 250 to 350°C, and then tended to constant at higher heat-treatment temperatures. While the phase content of FCC Ni had a near-linear increase from 250 to 700°C, and then kept unchangeable. The phase content of metastable Ni₅(P, Ni)₂ changed merely from 300 to 350°C,

afterwards it was almost a constant until the metastable phase disappeared at 700°C. For the amorphous phase, its content decreased monotonously with the increase of the heat-treatment temperature, and then the amorphous phase disappeared together with the metastable $\text{Ni}_5(\text{P},\text{Ni})_2$ at 700°C. At the lower-temperature ($\leq 300^\circ\text{C}$) crystallization stage of the amorphous Ni-P nanoparticles, it is clear that the amorphous phase was mostly transformed into crystalline Ni_3P , only a small portion was converted to crystalline Ni and $\text{Ni}_5(\text{P}, \text{Ni})_2$. While in the temperature range from 350 to 650°C, the remainder of the amorphous phase was mainly transformed into the crystalline FCC Ni. When the heat-treatment temperature increased from 650 to 700°C, the increment of Ni_3P content might due to the depletion of $\text{Ni}_5(\text{P}, \text{Ni})_2$. However, the augment of Ni content might be attributed to Ni precipitation from the amorphous phase.

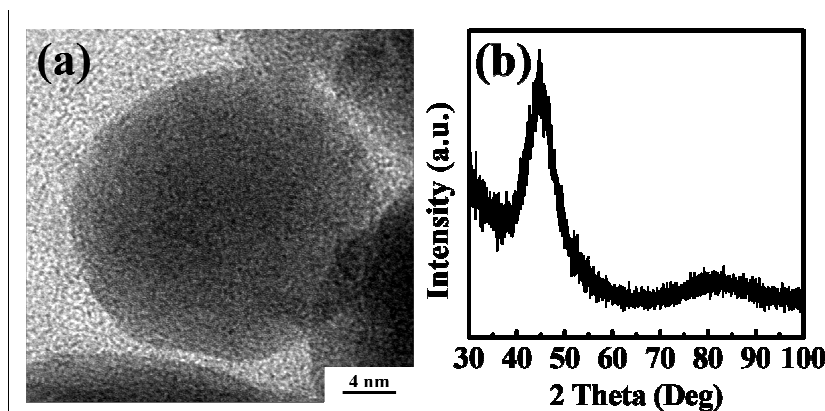


Figure 3. HRTEM image (a) and XRD pattern (b) of the as-prepared Ni-P nanoparticles before heat treatment. There is no observable long-range ordered clusters in the HRTEM image, indicating the amorphous attribute of the as-prepared Ni-P nanoparticles. Two very broad peaks around 45° and 83° confirm the amorphous nature of the as-prepared Ni-P nanoparticles.

More detailed structure changes were revealed by HRTEM images for specimens heated at different temperatures. Figure 3(a) shows the initial microstructure of the as-prepared Ni-P nanoparticles before heat treatment. This HRTEM image illustrates that the structure of the as-prepared Ni-P nanoparticles is basically disordered, there is

no observable long-range ordered nanodomains. A typical XRD pattern of the as-prepared Ni-P nanoparticles was also shown in Fig. 3(b). A relatively sharp peak centered at $2\theta = 44.5^\circ$ and a very broad peak ranging from 70 to 90° can be observed, which confirms the amorphous nature of the as-prepared Ni-P nanoparticles.

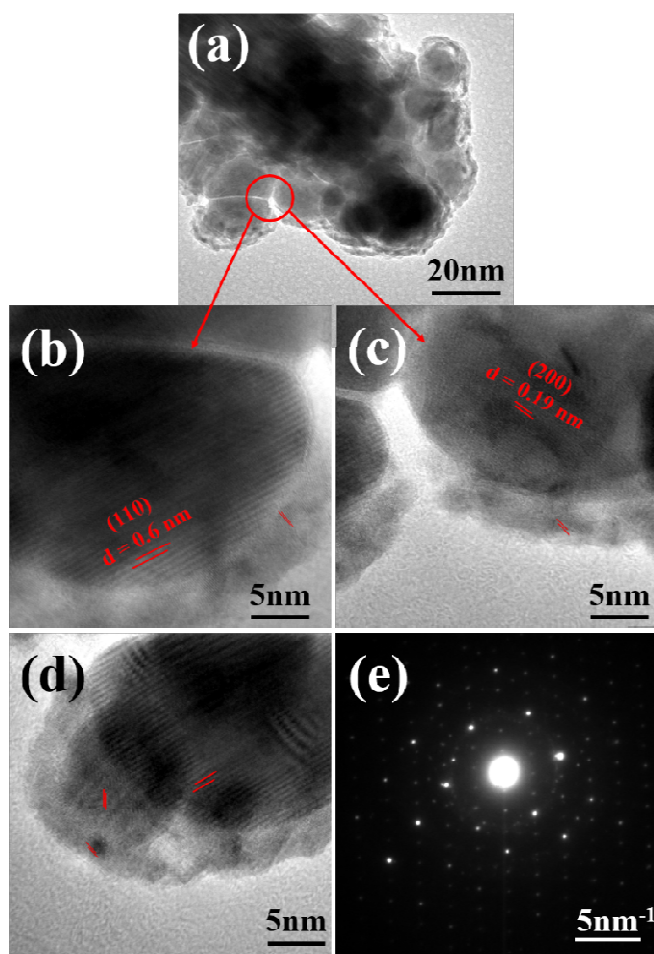


Figure 4. HRTEM pictures of the Ni-P nanoparticles annealed at 550°C . The nanoparticles are encapsulated with a thin shell as shown in (a). The d-spacings of the crystalline nanoparticles are about 0.6 nm or 0.19 nm, some tiny metastable-phase crystallites can be observed coexisting with the amorphous phase in the enclosed shell, as shown in (b) and (c). The overlap of nanoparticles with different crystalline structures can be observed in (d). Two sets of diffraction patterns from Ni_3P and Ni confirm that the sample is a mixture phases as shown in (e).

As the heating temperature increased, the phase and crystalline structure change correspondingly. To explore these changes, HRTEM pictures and electron diffraction patterns for the sample annealed at 550 °C were collected and shown in Fig. 4. Figure 4(a) shows that the bigger nanoparticles were enclosed with some thin “shell” after heat treatment at 550°C under Ar atmosphere. A location detail was enlarged in Fig. 4(b) and Fig. 4(c). Clearly, the d -spacing of the fringes in one nanoparticles is about 0.6 nm as shown in Fig. 4(b), which is corresponding to the (110) planes in the Ni₃P structure. The fringes with d -spacing of 0.19 nm was also found in another particle as shown in Fig. 4(c), which can be denoted as the (200) planes of FCC Ni. Figure 4(d) has also confirmed that particles with Ni₃P-rich phase are co-existed with particles with Ni-rich phase. Therefore, it is reasonable to assume that the as-prepared Ni-P nanoparticles were inhomogeneous due to different P contents, even though they looks the same with each other as just prepared. Particles with high P content will crystallized into Ni₃P-rich phases, and particles with low P content will grow into Ni-rich phases. Such inhomogeneity existed in Ni-P alloys was also reported before [26]. We also note that there is some fine fringes with random orientations in the enclosed shell as shown in Fig. 4(b) and 4(c). These tiny crystallites distributed inside in the shell are considered to be mainly the metastable phase Ni₅(P, Ni)₂. This metastable phase Ni₅(P, Ni)₂ and the amorphous phase coexist in the shell, which implies that the metastable phase is favorable to produce in the surface [10] of the nanoparticles. The existence of Ni₅(P, Ni)₂ was also reported elsewhere [27-30]. Small Area Electron Diffraction (SAED) pattern was also collected as shown in Fig. 4(e), showing two sets of overlapping diffraction patterns. The parallelogram pattern with large d -spacing is from the diffractions of the [6-31] zone axis of the tetragonal Ni₃P, while the rhombus pattern with small d -spacing is corresponding to the diffractions of the [0-11] zone axis of the FCC Ni.

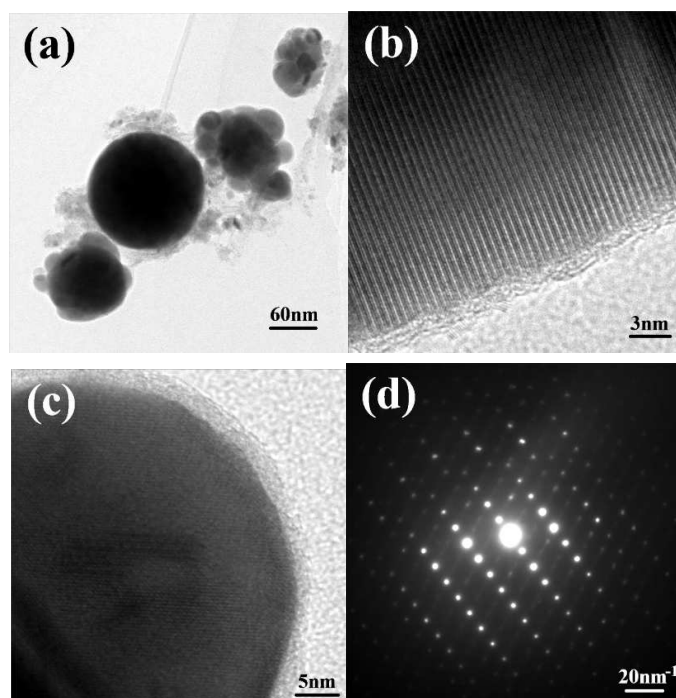


Figure 5. HRTEM pictures of the Ni-P nanoparticles annealed at 750°C. The particle morphology shows that some nanoparticles tend to aggregate into bigger particles and there are some smaller particles around the bigger ones as shown in (a). The bigger and smaller particles are, respectively, well-crystallized into Ni₃P and Ni, and a pretty thin amorphous layer can still be observed to enclose the crystalline particles as shown in (b) and (c), without the remainder of the metastable phase. The SAED patterns of the these nanoparticles confirm the well-ordered single-crystal structures of Ni₃P and FCC Ni nanoparticles.

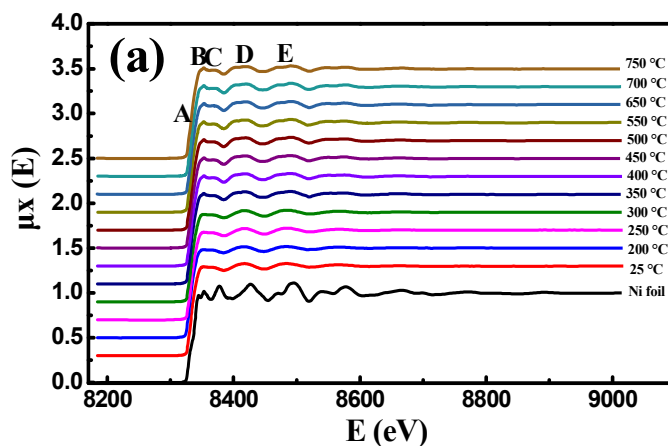
After the as-prepared Ni-P nanoparticles were totally grown into stable phases Ni₃P and Ni, the HRTEM pictures and electron diffraction patterns were collected to inspect their morphology and structure. Figure 5 is the TEM image corresponding to the specimen heated at 750°C for two hours. After heat treatment, some particles tend to aggregate together to form bigger particles (tens of nanometers). At the same time, there are some smaller particles (several nanometers) around the bigger ones as shown in Fig. 5(a). From the HRTEM picture of the margin of bigger particles, it seems that the bigger particles are single crystalline Ni₃P as shown in Fig. 5(b). From the

enlargement of small particles as shown in Fig. 5(c), the smaller particles are likely to be crystal Ni. The SAED pattern of these nanoparticles was shown in Fig. 5(d), which confirms the well-ordered single-crystal structure of the particles. There are two sets of diffraction patterns in Fig. 5(d). One has bright diffraction intensities, which can be attributed to the diffraction of [1-1-2] zone axis of FCC Ni crystal. Another has faint diffraction intensities, which can be attributed to the diffractions of [3-1-3] zone axis of Ni₃P crystal. From Fig. 5(b) and 5(c), a pretty thin amorphous layer with thickness less than 2 nm can still be found to enclose the well-crystallized nanoparticles. As comparing with that of the particles annealed at 550°C, the distinct reduction of the amorphous layer and the complete extinction of the metastable phase confirm the XRD results. Evidently, this HRTEM result also illustrates that the crystallization process could start from the interior of the as-prepared nanoparticles to the exterior.

3.2 Ni K-edge XAFS analysis

To extract the local structure changes of as-prepared Ni-P nanoparticles during the whole crystallization process, XAFS spectra from Ni K-edge were collected at Beamline 4B9A of BSRF. The XAFS data in energy-space, *R*-space, and *k*-space for the nanoparticles with different heat-treatment temperatures and a bulk Ni foil are shown in Fig. 6. No pre-edge peaks were observed in energy-space for all spectra of the specimens as shown in Fig. 6(a). This is due to the fact that the third orbitals are nearly full filled and only the less energetically favorable orbitals are able to receive a core 1s electron. Because the Fermi level is located between the energetically favorable orbitals (all occupied) and the partially empty and energetically unfavorable orbitals, the 1s to 3d transition will occur at different energies, depending on crystal field splitting [31]. There often are five features on the XANES spectrum of Ni K-edge. Feature A is partially hidden by the edge jump of the specimens, although it can be seen much clearly from the XANES spectrum of Ni foil. This feature is probably related to a 1s to 4s transition [32-35], which are enhanced for centrosymmetric environments. However, more detailed studies are required to

ascertain the origin of this feature, as it can be due to metallic Ni or a transition involving second neighbors nickel orbitals. Feature B is the white line of the Ni K-edge XANES spectra. For all the specimens of the Ni-P nanoparticle, feature B shifts to a higher energy as compared with that of Ni foil. This indicates the dominance of 1s to 4p transition atomic line mixing with P 3p orbitals [36]. Notably, the significantly broadening of the white line peak B can be attributed to the decrease in occupancy of 4d states [37]. This alteration from the bulk Ni spectrum suggests a change in geometric structure from octahedron to tetrahedron. Feature C, D, and the first EXAFS oscillation feature E can be observed when the sample was heated above 350 °C. This indicates the formation of long-range ordered nickel. With the increasing of the heating temperature, the XAFS spectra have hardly changed from 350 to 750 °C, indicating that the charge transfer, structure and phase types within Ni-P nanoparticles changed little in the following heat treatment. After removing the background, the total EXAFS functions with k^3 -weight were extracted from the X-ray absorption spectra for all the specimens as shown in Fig. 6(b). Roughly, these EXAFS functions of specimens with heat-treatment temperatures lower than 300 °C are very similar, having the monotonic oscillation characteristic of amorphous sample. When the specimens were heat-treated in the temperature range from 350 to 750 °C, their EXAFS oscillation are more complicated, confirming that the medium-range or the long-range ordered structures (i.e. crystallites) appear in the specimens.



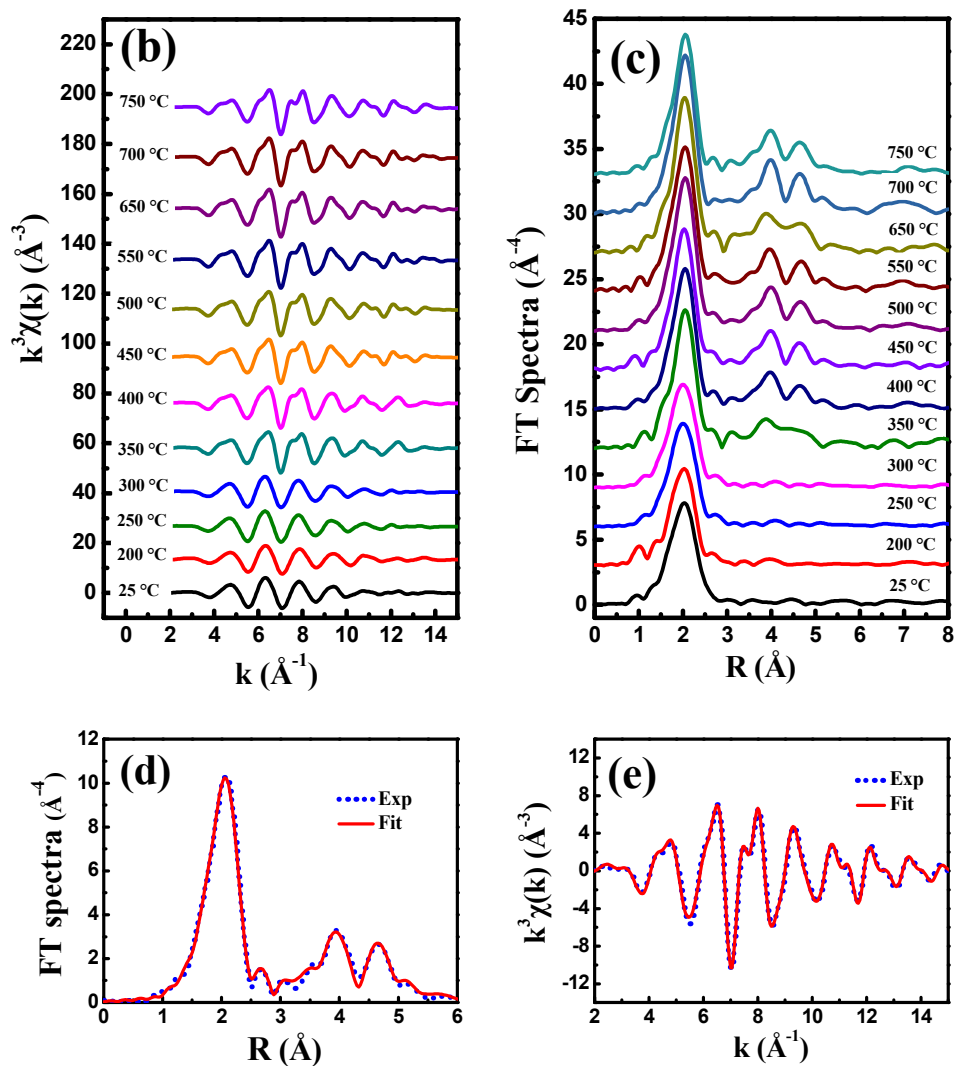


Figure 6. (a) X-ray absorption spectra of the Ni-P nanoparticles with different heat-treatment temperatures. (b) k^3 -weight EXAFS functions of all the Ni-P nanoparticles. (c) Fourier transforms spectra of EXAFS signals for all the Ni-P nanoparticles. (d) A typical EXAFS fitting in R -space for the specimen heated at 750°C. (e) A typical EXAFS fitting in k -space for the specimen heated at 750°C.

The crystallization process of the amorphous Ni-P nanoparticles can be directly observed from the R -space Fourier transformed (FT) spectra as shown in Fig. 6(c). The height of the first coordination peak centered around 2.1 Å directly increased from 7.9 to 10.6 when the heat-treatment temperature raised from 25 to 350°C.

Especially, the higher coordination peaks with larger R -values started to appear at 350°C, which is an indication that the amorphous sample initiates the crystallization process [38] with medium-range order. This change was also confirmed by the XRD patterns as shown in Fig.1, where the diffraction peaks of crystalline Ni₃P and FCC Ni started to appear at 300~350°C. Although the diffraction peaks of Ni₃P can be observed from the sample with heat-treatment at 300°C, its tiny crystallite size limits the appearance of higher coordination shell at the FT spectra. When the heat-treatment temperature increases from 350 to 650°C, the first coordination peak has a little increase in height from 10.6 to 11.9, but has no change in position. While the higher coordination peaks have continuous increase in heights, and are obviously split into two peaks at 400°C. The two separated higher coordination peaks suggest that the medium-range or long-range ordered crystalline structures have been formed. The above XRD results demonstrate that the phase change from amorphous Ni-P nanoparticles to Ni₃P crystallites was accompanied by the incessant precipitation of crystalline Ni clusters. However, the precipitation rate of FCC Ni is much higher than the growth rate of Ni crystallites, resulting in that the number of Ni crystallites increases faster than their size increase before the amorphous matrix was completely exhausted. From 700 to 750°C, it is near the end of the crystallization process of the amorphous specimen. The surplus Ni atoms were continuously precipitated from the amorphous matrix as it was changed into Ni₃P crystallites. On the one hand, the precipitated Ni atoms were attached to the formed Ni clusters. On the other hand, the formed Ni clusters agglomerated together and formed more perfect Ni crystallites. Therefore, the higher coordination peaks in R -space intensified correspondingly, and the oscillation amplitude in k -space amplified as well. These changes in Ni K-edge XAFS spectra are in accordance with those in XRD patterns shown in Fig. 1.

To extract accurate parameters for the atoms surrounding the central Ni atoms, the EXAFS spectra of the annealed specimens at different temperatures were fitted both in R -space and k -space. The EXAFS fitting curves in R -space and in k -space for the annealed specimen at 750°C were shown in Fig. 6(d) and 6(e), respectively. During the EXAFS fitting with the Demeter software package, scattering pathways

from the combination among Ni, Ni₃P and Ni₁₂P₅ crystalline structures were tested. However, the combination of Ni + Ni₁₂P₅ or Ni + Ni₃P + Ni₁₂P₅ could only fit well the first coordination peak. When the fitting range was extended to more than 4 Å in *R*-space, the fitting results are not acceptable. Therefore, a combination of scattering pathways from only Ni and Ni₃P crystal structures were used as the theoretical models. These scattering pathways were calculated through FEFF8 code embedded in Demeter software. Figure 7 shows the fitting parameters for the first coordination shell in the full-spectrum fitting. The theoretical parameters extracted from FCC-Ni and Tetrahedrally Close-Packed (TCP) Ni₃P models are also shown in Fig. 7 and designated as dot lines for simplifying the comparison between theoretical values marked with subscript “T” and experimental data marked with subscript “E”. From Fig. 7(a), it can be seen that the Ni-Ni coordination number is much smaller than the theoretical value 12 of the FCC-Ni model. This result implies that Ni atoms in this specimen were contained in at least two phases [38]. The possible Ni-species could be FCC-Ni, disordered Ni, short-range ordered Ni clusters, and TCP-Ni₃P in our case. However, when the sample was heat-treated at 700 and 750 °C, XRD and TEM results confirm that the final products are FCC-Ni and TCP-Ni₃P. Based on the EXAFS fitting results, the contents of FCC-Ni at 700 and 750°C were calculated to be 44.2% and 44.3%, which are in good agreement with the calculated values from XRD patterns. While the coordination numbers of Ni-Ni and Ni-P atom-pairs in the TCP-Ni₃P phase is very close to the theoretical values as shown in Fig. 7(a) and 7(b). This result implies that the average Ni-P environment in the specimens is similar to the Ni₃P crystal, even if a small quantity of metastable phases Ni₅(P, Ni)₂ coexists with the crystalline Ni₃P in the specimen at the lower heat-treatment temperatures. It should be noticed that the obtained coordination numbers, including the bondlengths, the standard deviation of $\Delta R/R$, and Debye-Waller factors for the samples with heat-treatment temperature around 300 °C as shown in Fig. 7(c), 7(d), 7(e), and 7(f) all have an obvious departure from the changing trend with heat-treatment temperature. This singularity can be attributed to the nucleation growth of the crystalline phases from the amorphous matrix as confirmed by the XRD patterns,

which results in a larger structural alteration at the initial nucleation stage.

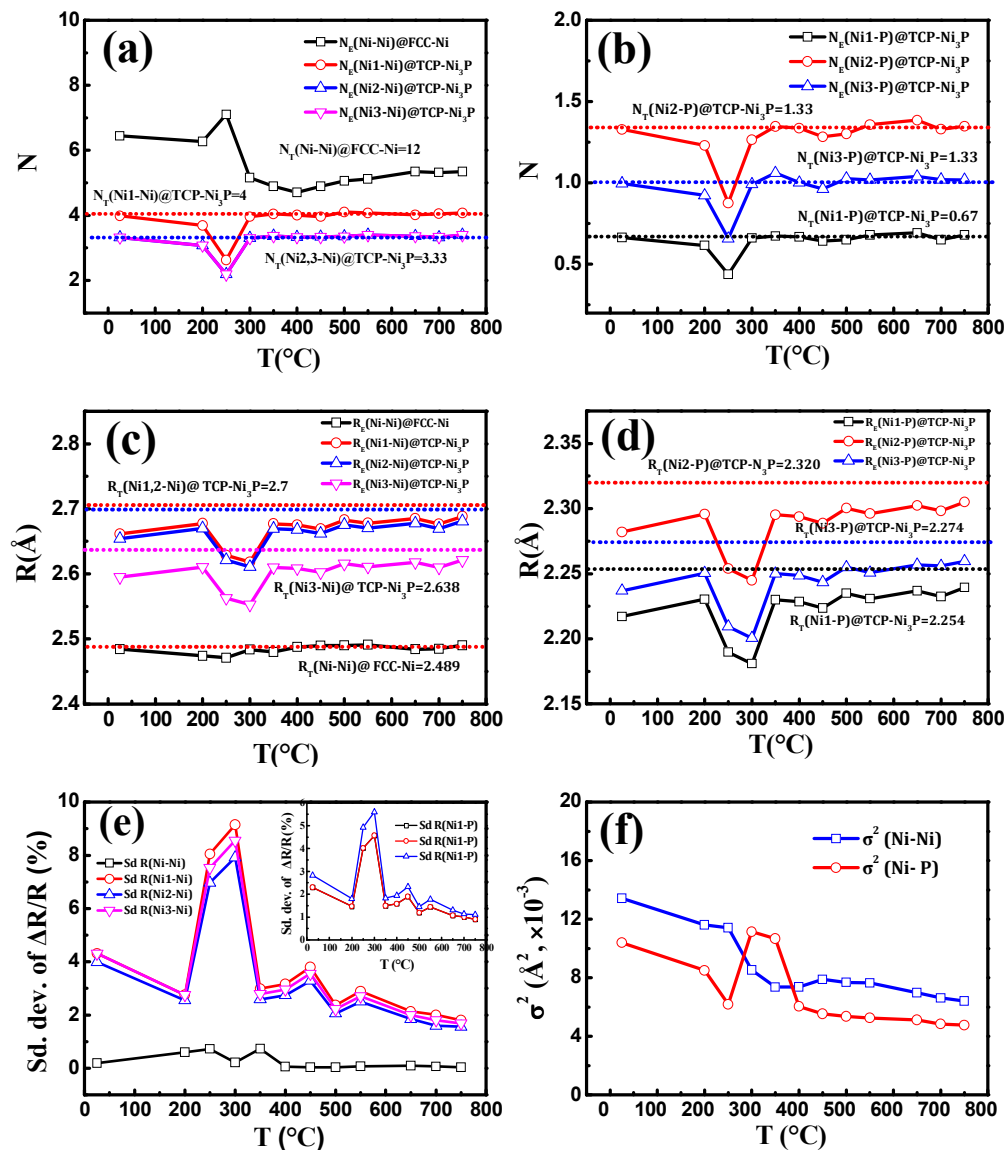


Figure 7. Structure parameters extracted from the fitting results using theoretical Ni and Ni₃P crystalline structure models. (a) Variation of Ni-Ni coordination number with heat-treated temperature in FCC-Ni and TCP-Ni₃P crystallites. (b) Variation of Ni-P coordination number with heat-treated temperature in FCC-Ni and TCP-Ni₃P crystallites. (c) Variation of Ni-Ni bondlengths with heat-treated temperature in FCC-Ni and TCP-Ni₃P crystallites. (d) Variation of Ni-P bondlengths with heat-treated temperature in FCC-Ni and TCP-Ni₃P crystallites. (e) Stand Deviation of $\Delta R/R$ deviated from theoretical bondlengths. (f) Variation of Debye-Waller factors

with heat-treatment temperature for the average Ni-Ni and Ni-P atom-pairs. Ni1, Ni2, and Ni3 represent the three inequivalent 8g sites occupied by Ni atoms in the TCP-Ni₃P crystal. Subscripts “E” and “T” represent, respectively, the experimental and theoretical values.

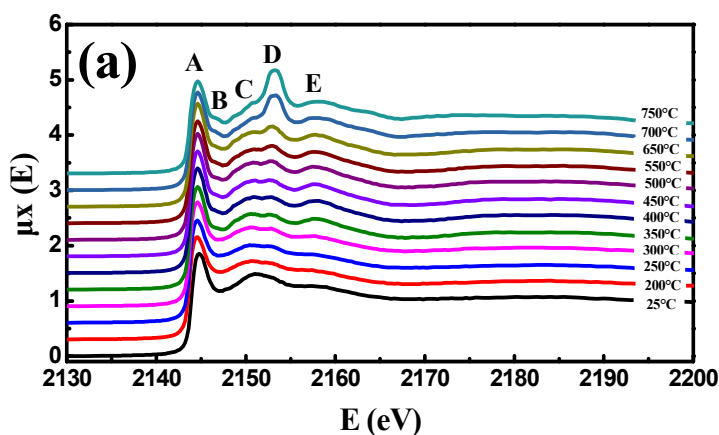
The Ni-Ni and Ni-P bondlengths of specimens annealed at different temperatures were shown in Fig. 7(c) and 7(d). The Ni-Ni bondlengths in the FCC-Ni crystallites have almost the same value with bulk FCC-Ni except a little decrease around 250°C, while the Ni-Ni coordination number from FCC-Ni increased to 7.1 at 250°C. This is probably because of the precipitation of short-ordered FCC-Ni clusters from the amorphous matrix. This precipitation of FCC-Ni clusters resulted in the formation of new Ni-P bonds in the form of Ni₃P clusters in the amorphous matrix. Since the Ni-P bondlength doped in FCC-Ni cluster is longer than that in the TCP-Ni₃P cluster, the breakdown of Ni-P bonds in FCC-Ni and subsequent formation of Ni-P bonds in TCP-Ni₃P make the average bondlength of Ni-P decreased continuously from 200 to 300°C. As the heating temperature increased, a large amount of Ni₃P with long-range ordered structure formed, leading to the elongation of Ni-Ni and Ni-P bondlengths. Once the long-rang ordered Ni₃P crystals are formed, the Ni-Ni and Ni-P bondlengths belonging to the first shells changed hardly from 350 to 750°C. Figure 7(e) showed the deviation of the measured bondlength R_E from the theoretical R_T in the form of root mean square. Due to the precipitation of FCC-Ni clusters from the amorphous matrix and the formation of TCP-Ni₃P clusters in the amorphous matrix, the atoms in the matrix were relatively more disordered than atoms in the FCC-Ni clusters at these heating temperatures of 250 and 300°C. In addition, due to the decomposition and re-formation of Ni-Ni and Ni-P bonds, the atoms at these heating temperatures of 250 and 300°C were much more disordered than at other heating temperatures. Therefore, the standard deviation of $\Delta R/R$ (Std. dev. of $\Delta R/R$) values at 250 and 300°C are apparently higher than those at other temperatures, but it is relatively small in the FCC-Ni clusters than in the others. This disorder has also been displayed in the form of the average Debye-Waller factors (σ^2) as shown in Fig. 7(f).

The good fitting results using only Ni and Ni₃P crystal structures also illustrate that the clusters contained in the specimen, either short-range order or long-range order, have structures of FCC-like Ni and TCP-like Ni₃P. That is, the atoms in the noncrystalline matrix are not totally disordered but have short-range ordered structures of FCC-like Ni or TCP-like Ni₃P crystals. This kind of short-range ordered structures are much of the same with long-range ordered counterparts, except at the transformation point, such as 250°C. As the amorphous part of the specimen has the same short-range order with the crystalline phases, it is difficult to set them apart from the crystalline phases during the EXAFS fitting. However, another metastable phase was not included in our fitting process despite the good fitting results. That is to say, the EXAFS cannot be used to distinguish a phase with content as low as 2% from a mixture of phases with different structures in our case.

3.3 P K-edge XAFS analysis

P K-edge XANES spectra have been demonstrated as an excellent way to examine phosphorus mineralogy and transformations in natural and agricultural systems [39-43]. To further determine the local structure variations around P atoms in the specimens after heat treatment at different temperatures, the P K-edge X-ray absorption spectra were collected in fluorescence mode. Normalized P K-edge X-ray absorption spectra are shown in Fig. 8(a). There are five features A, B, C, D, and E on the XANES spectra. All the XANES spectra exhibit a sharp intense resonance (white line) designated as feature A, which was resulted from electronic transitions of the core electrons into unoccupied p-like valence electronic states in the conduction band, specifically, 1s to π^* transition from a P 1s to a hybrid orbital. It has been reported that the intensity, energy position and line shape of sharp white line are determined by the electronegativity, the number of the nearest neighbors, the size and the symmetry of the coordination polyhedron around the absorb atom [43-45]. For these specimens studied here, the energy positions of P K-edge exhibit a slightly blue shifts with the raising of the heat-treatment temperature, indicating that the valence-charge transfer

and the slight change of chemical bonds. However, the intensity of feature A is almost unchangeable until the heating temperature increase to 650°C. When the heating temperature increased from 650 to 750°C, the intensity of feature A decreases from 1.91 to 1.68, which is probably due to the slight charge transfer from P to Ni [46]. Feature B is a weak resonance feature, it appears on the XANES spectra only when the specimen was heat-treated above 300°C. Feature B of P K-edge in XAFS measurements and the diffraction peaks of crystalline phases in XRD measurements appeared almost at the same heating temperature (300-350°C). This coincidence implies that feature B might be related to the crystalline structures of Ni₃P. Feature C located at 2151.4 eV appeared on all the XANES spectra of the specimen with different heat-treatment temperatures, but the as-prepared specimen without heating treatment has the most outstanding feature. Therefore, feature C is probably related to the average near-neighbor structure in the specimens. However, feature D almost cannot be observed from the initial amorphous specimen. With the increase of the heat-treatment temperature, feature D increased slightly from 200 to 650°C, and then increased sharply from 700 to 750°C. Evidently, feature D is strongly dependent on the crystalline structures. Similar to feature C, feature E also always appeared on all the XAFS spectra, it can be attributed to the average near-neighbor structures of the specimens at different heat-treatment temperatures.



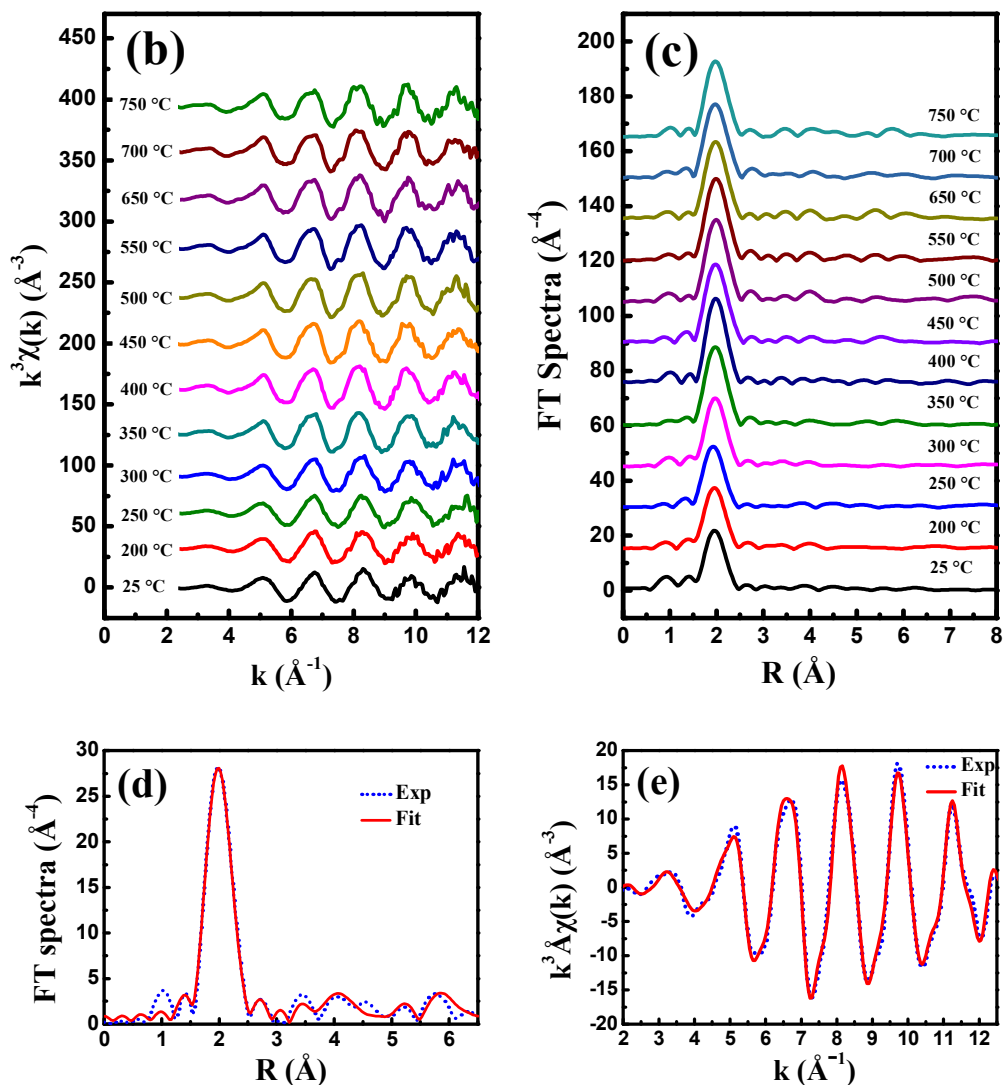


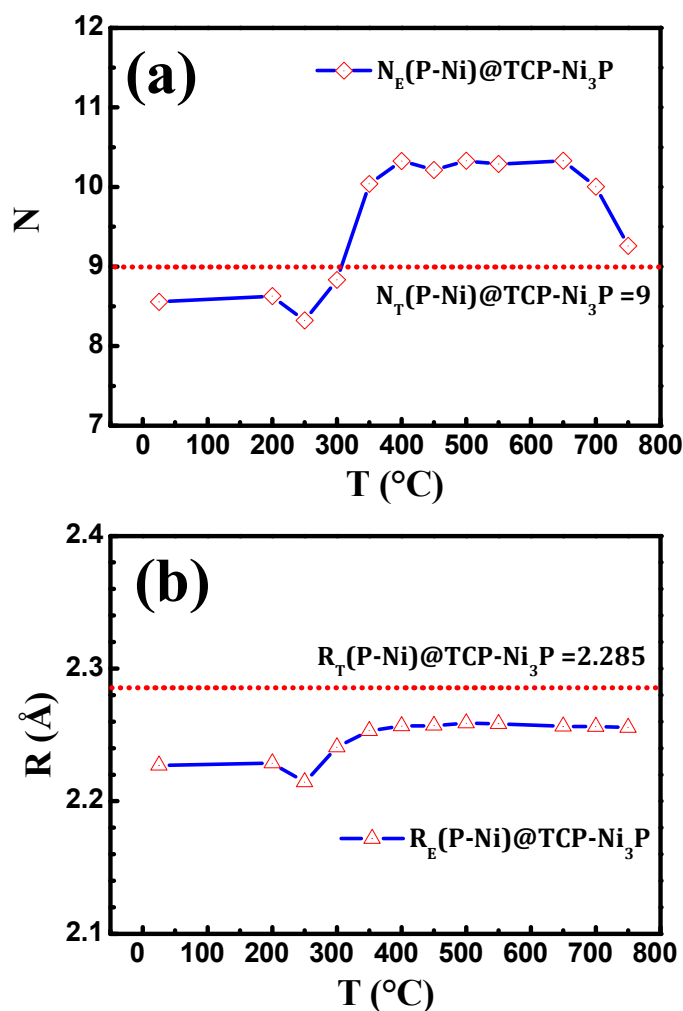
Figure 8. (a) P K-edge X-ray absorption spectra measured in fluorescence mode. (b) P K-edge k^3 -weight XAFS functions of the specimens at different heat-treatment temperatures. (c) Fourier transforms spectra of the P K-edge k^3 -weighted EXAFS functions. (d) A typical fitting curve of the EXAFS signal in R -space for the specimen heated at 750 °C. (e) A typical fitting curve of the EXAFS signal in k -space for the specimen heated at 750 °C.

After removing the background of the P K-edge X-ray absorption spectra, the k^3 -weight EXAFS oscillations $k^3\chi(k)$ were extracted for all the Ni-P nanoparticles with different heat-treatment temperatures as shown in Fig. 8(b). It is found that all

the P K-edge XAFS oscillations are quite similar to each other. This result means that the average local atomic structure around P centers is very similar in all the specimens with different heat-treatment temperatures. This similarity of the P K-edge XAFS oscillations is because the P atoms are mainly in the amorphous matrix as the heat-treatment temperature is below 300 °C, or in the crystalline Ni₃P phase as the heat-treatment temperature is over 300°C. The FT spectra of these XAFS oscillations are shown in Fig. 8(c). It can be seen that there is only one distinguishable coordination peak centered around 2.0 Å, corresponding to the first P-Ni bond with a bondlength of about 2.23 Å (Phase shift has not been corrected in all spectra). As the heating temperature increased from 25 to 250°C, this coordination peak had a slight increase in height. This slight enhancement of the coordination peak can be attributed to the nucleation of the short-ordered Ni₃P clusters. Comparing the magnitude change of coordination peak in FT spectra with the feature change of XANES spectra, it can be concluded that the XANES spectra in energy space are much more sensitive than the FT spectra to characterize the nucleation of short-ordered clusters from the amorphous matrix. The appearance of feature D could be used as a characteristic of the Ni₃P crystalline phase formation. However, feature D in energy has only a slight increase from 300 to 400 °C, but the coordination peak in *R*-space increases sharply in the same temperature range. This rapid formation or precipitation of crystalline TCP-Ni₃P and FCC-Ni phase have been also characterized by XRD patterns through the intensify of diffraction peaks during this temperature range. This phenomenon demonstrates that the FT spectra are more sensitive than the XANES spectra to the formation and precipitation of crystalline phases. From 450 to 750 °C, the coordination peak in *R*-space changes hardly, indicating that the local structures of Ni₃P became stable when the heating temperature reached to 400°C. But the feature D in energy space has a remarkable increase, indicating that the crystalline structures get more perfect. Therefore, it can be concluded that the XANES spectra in energy space is more sensitive than the FT spectra in *R*-space to the growth of crystallites.

To extract local structure parameters around P atoms, the P K-edge XAFS spectra were fitted using the program “Artimis”, one of the Demeter software packages.

Scattering pathways from Ni_3P crystal structures were used as the theoretical models. In order to consider the contribution of the metastable phase to the XAFS spectra, partial scattering pathways from Ni_{12}P_5 around 4.3 \AA were also included in the fitting. The goodness of fits using theoretical model Ni_3P and part of Ni_{12}P_5 for all the samples implies that P atoms contained in the Ni-P nanoparticles were mainly in the form of Ni_3P , despite of the existence of the XRD detectable metastable phase and the amorphous phase. The use of additional pathways from Ni_{12}P_5 during the fitting process indicates that the crystalline structure of Ni_3P has been distorted. However, this distortion could not be detected through Ni K-edge XAFS spectra due to its low phase content. The fitting curves in R -space and in k -space for the sample with heat-treatment temperature at $750 \text{ }^\circ\text{C}$ are, respectively, shown in Fig. 8(d) and 8(e).



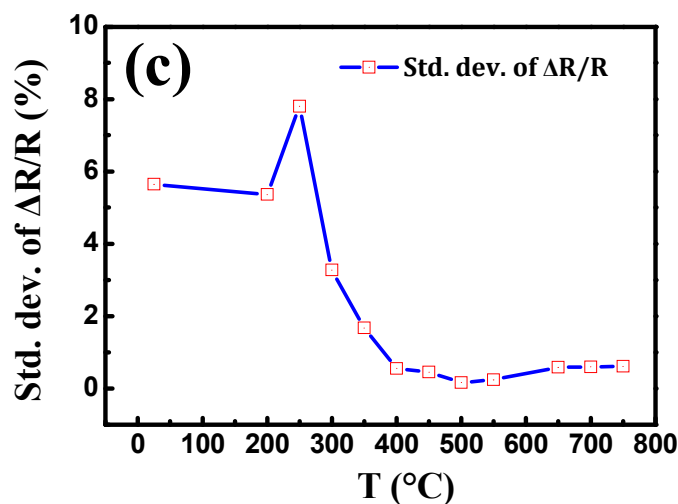


Figure 9. Near-neighbor fitting parameters of the P K-edge XAFS spectra for all the specimens with different heat-treatment temperatures. (a) Average change of P-Ni coordination numbers with heat-treatment temperature. (b) Average change of P-Ni bondlengths with heat-treatment temperature. (c) Standard deviation of $\Delta R/R$ of the fitting bondlength from the theoretical values. Theoretical coordination number and bondlength from Ni_3P crystal are presented as the dot lines.

Figure 9 shows the fitting parameters for the near-neighbors of all the specimens at different heat-treatment temperatures. The changes of P-Ni coordination number and bondlength with heat-treatment temperature are, respectively, shown in Fig. 9(a) and 9(b), the standard deviation deviation of P-Ni bondlength from the theoretical value is shown in Fig. 9(c). It is clear that from room temperature to 200°C, the P-Ni coordination number and bondlength are all smaller than the theoretical values from Ni_3P crystal, indicating that the Ni_3P -like clusters have not been well formed in the amorphous matrix. The larger standard deviation of ($\Delta R/R$) values in Fig. 9(c) also confirmed this point. When the heating temperature increased to 250 °C, both the P-Ni coordination number and bondlength decreased further, accompanied with the increase of the standard deviation of ($\Delta R/R$) values. The same change trend has been observed from the Ni K-edge XAFS fitting spectra. Those changes illustrate that a much more disordered phase has been undergoing during the crystallization process

from disordered amorphous phase to ordered crystalline phase. This much more disordered phase stage occurred at 250 °C in our case, just before the appearance of diffraction peaks at 300°C. Therefore, we conclude that a much more disordered stage proceeded before the XRD detectable crystalline phase was formed. With the increase of heating temperature, the average P-Ni coordination number began to increase continuously and remained stable around 10. While the average P-Ni bondlength evolved in the same manner, except that their values were little smaller than the average theoretical P-Ni bondlength in Ni₃P crystal. These were due to the appearance of the Ni-rich metastable phase compared with Ni₃P. However, the nearest-neighbor P-Ni bondlength is in similarity with that of Ni₃P. When the heating temperature reached to 700 °C, the P-Ni coordination number began to decrease, and finally reached to the theoretical value in Ni₃P at 750°C due to the exhaustion of the Ni-rich metastable phase. These results illustrate that the metastable phase has little effect on the nearest-neighbor P-Ni bondlength. Probably, It is because the nearest-neighbor P-Ni bondlength in the metastable phase is much of the same with that of Ni₃P. The Standard deviation of $\Delta R/R$ values decreased gradually from 250 to 400°C, and then remained almost stable from 400 to 750°C. Taking into consideration of crystallization behavior characterized by XRD patterns, we found that there was a threshold of the standard deviation of $\Delta R/R$ during the phase transformation from amorphous phase to crystalline phase. When the standard deviation of $\Delta R/R$ was below 0.61%, the Ni₃P phase in the mixture has a well-developed crystalline structure. When the standard deviation of $\Delta R/R$ was between 0.61% to 3.27%, it indicates that the Ni₃P phase was growing into crystalline phases, but its structure was not well developed. When the standard deviation of $\Delta R/R$ was higher than 5.36%, the phase which has a Ni₃P-like structure was defined as amorphous from XRD patterns.

3.4 Magnetic properties

The magnetic properties of the nanoparticle samples were analyzed at room temperature using Vibrating Sample Magnetometer (VSM) with an applied field, -15

$kOe \leq H \leq 15 kOe$. Figure 10(a) shows the magnetization versus applied-field (M vs. H) hysteresis loops for the samples annealed at different temperatures and Figure 10(b) presents the saturated magnetic moment (M_s) values. The hysteresis loop for Ni powders is also presented in Figure 10(c) for comparison. The very low saturated magnetic moment (0.021 emu/g) for the sample without heat treatment suggests that the as-prepared amorphous Ni-P nanoparticles was non-magnetic materials. Similar results were also reported for amorphous Ni-P alloys with high P contents [16, 26, 47]. Even when the heating temperature increased to 200 °C, the M_s value of this sample increases such a little that the hysteresis loop curve is nearly overlapped with that of the sample without heat treatment, indicating that the local structure of Ni-P nanoparticles has changed hardly. This has also been confirmed by the XAFS spectra from both Ni and P k-edge besides the XRD patterns. However, when the heating temperature increased to 250 °C, the M_s value increased to 0.490 emu/g, despite of the amorphous nature of the Ni-P nanoparticles determined by its XRD pattern. That is, the clusters within the particles have already exhibited properties similar with bulk crystalline phase, while they could not be detected by traditional XRD and TEM techniques. The saturated magnetic moment of the Ni-P nanoparticles is mainly proportional to the quantity of the crystalline Ni in the sample, as Ni_3P phase exhibits a temperature-independent Pauli paramagnetic [48] and the Ni_5P_2 phase is likely to be paramagnetic due to its high P content [47]. Therefore, the increase of M_s value for the sample annealed at 250°C is attributed to the formation of FCC-Ni. The increase of Ni-Ni coordination number from Ni K-edge XAFS has also confirmed this point. As the heating temperature increased from 250 to 350 °C, the saturated magnetic moment increased sharply due to the precipitation of FCC-Ni phase from the amorphous matrix. The diffraction peaks for FCC-Ni phase as shown in Fig. 1 grew from broadened peaks to apparent sharp peaks during this heating temperature range, indicative of the formation of FCC-Ni phase. The intensified first-shell peaks in R-space of Ni K-edge XAFS spectra have also verified the growth of FCC-Ni phase. As the Ni content increased, the saturated magnetic moment of the annealed samples increased correspondingly. And finally, the M_s value reached to maximum due to the

growth halt of FCC-Ni phase.

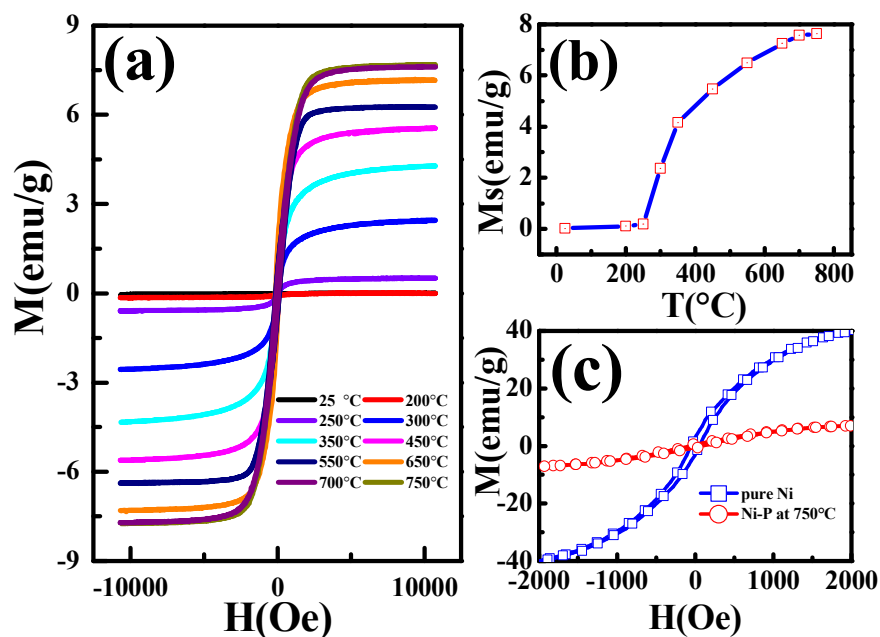


Figure 10. Magnetization vs. applied field hysteresis loops measured at room temperature. (a) M-H hysteresis loops for the samples annealed at different temperatures. (b) Saturated magnetic moment (M_s) of the samples annealed at different temperatures. It shows a sharp increase at first and then reach to a peak of 7.75 emu/g after the sample was heated to 750°C, presenting a positive correlation with the content of FCC-Ni phase. (c) Comparison of M-H hysteresis loops between Ni powders and the sample annealed at 750°C. Clearly, all the samples exhibit significantly decreased magnetization as compared with Ni powders, due to effect of phosphorus.

3.5 Crystallization mechanism

Through the analysis of XRD patterns, HRTEM pictures and XAFS spectra, a clear picture on the crystallization behavior of the as-prepared amorphous Ni-P nanoparticles has been presented. Although the as-prepared Ni-P nanoparticles appears no difference before heat treatment, they are actually a mixture of low-P nanoparticles and high-P nanoparticles. Figure 11 depicts the whole crystallization

behavior of the as-prepared amorphous Ni-P nanoparticles. For high-P nanoparticles as shown in Fig. 11(a), the crystallization process was divided into three stages. In Stage I, P atoms precipitated gradually from P-doped FCC-Ni clusters, resulting in the formation of pure FCC-Ni clusters. Afterwards, the precipitated P atoms diffused outward to form Ni₃P clusters and metastable phase Ni₅P₂ in the Ni-rich zone and near the edge of the nanoparticles. With the heating temperature increasing, the formed clusters grew into crystalline phases correspondingly and can be detected by XRD as TCP-Ni₃P, FCC-Ni, and metastable phase. The appearance of apparent diffraction peaks indicates the beginning of crystallization Stage II. In this stage, the growth rate of individual phases varies differently. Crystalline Ni₃P clusters grow rapidly into long-range ordered Ni₃P crystallites, then remain almost unchanged even though the heating temperature increased continuously. While the growth of crystalline Ni is quite slow compared with Ni₃P. It is worth notice that the metastable phase was merely changed during the whole stage, implying that the metastable phase existed mostly between Ni₃P and Ni clusters served as a transition zone. After the depletion of amorphous matrix, the crystallization process gets into Stage III. Metastable phase was also disappeared due to its decomposition into Ni₃P and Ni. Finally, Ni-P nanoparticles were developed into crystalline structures of Ni₃P and Ni, with crystalline Ni at the edge of the particle. Based on the XRD, TEM and XAFS analysis results, it seems no difference between the as-prepared Ni-P nanoparticles with high-P and low-P contents, due to the distortion of FCC-Ni crystalline lattice resulting from the entry of P atoms. However, as for the low-P nanoparticles, the crystallization process is relatively simple as shown in Fig. 11(b). Unlike the crystallization behavior of particles with high-P content in Stage I, the outward P atoms from FCC-Ni crystalline lattice combined with single Ni atoms into only Ni₃P clusters rather than both Ni₃P clusters and metastable phase. As the crystallization gets into Stage II, dispersed Ni clusters and Ni atoms connected with each other forming large crystalline Ni clusters with the same crystalline structure of bulk FCC-Ni. While, the clusters of Ni₃P grow a little bit due to the limitation of P atoms. In addition, after the crystallization of both the two kinds of nanoparticles, they tend to merged together as

shown in Fig. 5(a). This is probably due to the large surface tension of small particles.

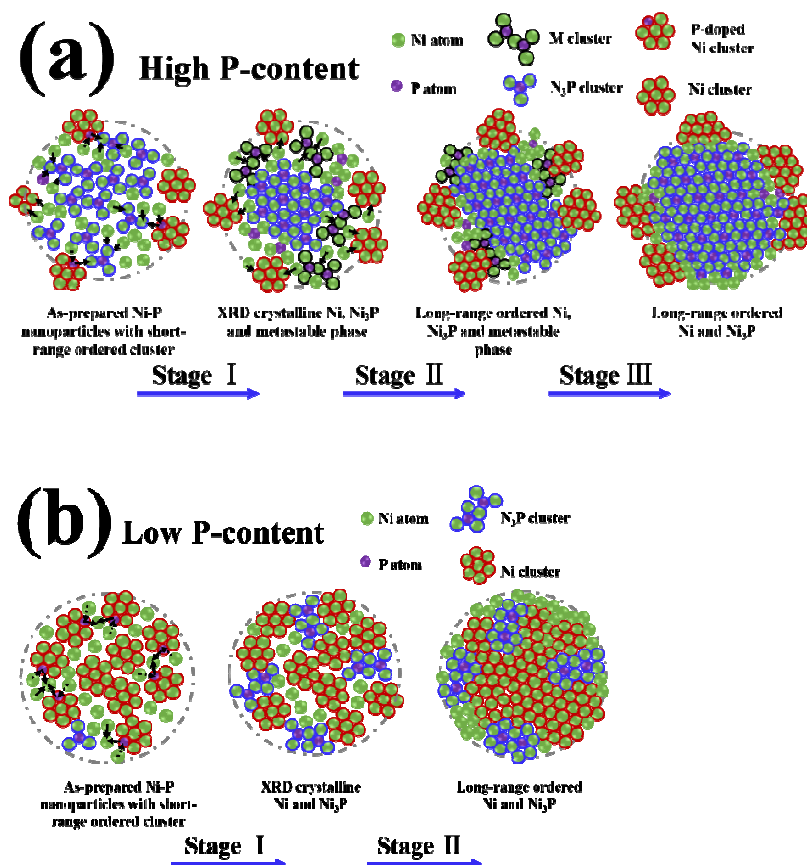


Figure 11. Crystallization behavior of Ni-P nanoparticles with high-P content (a) and low-P content (b). Three stages were used to clearly describe the crystallization of high-P amorphous Ni-P nanoparticles due to the appearance of metastable phase. The crystallization of low-P nanoparticles is relatively simple. The XRD-amorphous Ni-P nanoparticles with low-P content were directly transformed into Ni₃P and Ni crystalline phases.

4. Conclusion

The crystallization behavior of as-prepared amorphous Ni-P nanoparticles has been investigated through XRD, HRTEM, Ni K-edge and P K-edge XAFS. The results demonstrate that TCP-Ni₃P, metastable phase, and FCC-Ni occurred simultaneously. TCP-Ni₃P and the metastable phase grew faster than FCC-Ni. Once

the TCP-Ni₃P and the metastable phase are formed, they grow rapidly into XRD detectable crystalline phases. While the FCC-Ni phase precipitated gradually from the amorphous matrix. FCC-Ni and TCP-Ni₃P are the main phases within the particles, while the metastable phase presented as coated shell in the outside of the particles. At the end of the crystallization process, only TCP-Ni₃P and FCC-Ni were observed. P atoms precipitation from P-doped FCC-Ni at the beginning of the crystallization was concluded from the XAFS fitting results both from Ni K-edge and P K-edge. The metastable phase has little effect on the local structure of Ni-P nanoparticles during the crystallization process. However, it plays an important role on the electronic states transition within Ni₃P phase. The magnetization of the samples annealed at different temperatures came from pure FCC-Ni within the particles, and the saturated magnetic moment was found to be in proportional to the Ni content of the particles.

The work illustrates that XAFS is very sensitive to local structure changes before the samples transformed into XRD crystalline phases. However, the XAFS spectra changed hardly when the crystalline phases continued to growth. In the contrary, the diffraction peaks in XRD patterns intensified significantly due to the continued growth of the crystalline phases. Therefore, these two techniques should be paired together in order to obtain a complete characterization of both local atomic structure and long-range ordered structure.

Acknowledgement

This work was supported by National Natural Science Foundation (Nos. 51374019, U1232203, 10835008, 50374010) of China.

References

- [1] Martyak, N. M. *Chem. Mater.* 1994, **6**, 1667.
- [2] Lambert, M. R.; Duquette, D. J. *Thin Solid Films* 1989, **177**, 207.
- [3] Mal, Q. X.; Daniels, R. D.; Harpalani, H. B. *Thin Solid Films*, 1988, **166**, 235.
- [4] Kumar, P. S.; Nair, P. K. *J. Mater. Process. Technol.* 1996, **56**, 511.
- [5] Agarwala, R. C.; Ray, S. Z. *Metallkd.* 1988, **79**, 472.
- [6] Allen, R. M.; Vander Sande, J. B. *Scr. Metall.* 1982, **16**, 1161.
- [7] Martyak, N. M.; Drake, K. *J. Alloy. Compd.* 2000, **312**, 30.

- [8] Kenog, K. G.; Sha, W.; Malinov, S. *J. Mater. Sci.* 2002, **37**, 4445.
- [9] Keong, K. G.; Sha, W.; Malinov, S. *Acta Metall. Sin. (Eng. Lett.)* 2001, **14**, 419.
- [10] Hur, K. H.; Jeong, J. H.; Lee, D. N. *J. Mater. Sci.* 1990, **25**, 2573.
- [11] Xie, S. H.; Qiao, M. H.; Zhou, W. Z.; Luo, G.; He, H. Y.; Fan, K. N.; Zhao, T. J.; Yuan, W. K. *J. Phys. Chem. B.* 2005, **109**, 24361.
- [12] Kenog, K. G.; Sha, W.; Malinov, S. *J. Alloy. Compd.* 2002, **334**, 192.
- [13] Bunker, G. *Introduction to XAFS*, Cambridge University Press, 2010.
- [14] Cheng, G. J.; Carter, J. D.; Guo, T. *Chem. Phys. Lett.* 2004, **400**, 122.
- [15] Moreau, L. M.; Ha, D. H.; Bealing, C. R.; Zhang, H. T.; Hennig, R. G.; Robinson, R. D. *Nano Lett.* 2012, **12**, 4530.
- [16] Moreau, L. M.; Ha, D. H.; Zhang, H. T.; Hovden, R.; Muller, D. A.; Robinson, R. D. *Chem. Mater.* 2013, **25**, 2394.
- [17] Yao, T.; Sun, Z. H.; Li, Y. Y.; Pan, Z. Y.; Wei, H.; Xie, Y.; Nomura, M.; Niwa, Y.; Yan, W. S.; Wu, Z. Y.; Jiang, Y.; Liu, Q. H.; Wei, S. Q. *J. Am. Chem. Soc.* 2010, **132**, 7696.
- [18] Stern, E. A. *Contemp. Phys.* 1978, **19**, 289.
- [19] Tan, Y. Y.; Sun, D. B.; Yu, H. Y.; Wu, T.; Yang, B.; Gong, Y.; Yan, S.; Du, R.; Chen, Z. J.; Xing, X. Q.; Mo, G.; Cai, Q.; Wu, Z. H. *J. Alloy. Compd.* 2014, **605**, 230-236.
- [20] Ravela, B.; Newville, M. *J. Synchrotron Radiat.* 2005, **12**, 537.
- [21] Rehr, J. J.; Kas, J. J.; Vila, F. D.; Prange, M. P.; Jorissen, K. *Phys. Chem. Chem. Phys.* 2010, **12**, 5503.
- [22] Ravel, B.; Kelly, S. D. *AIP Conf. Proc.* 2007, **882**, 150.
- [23] Oryshchyn, S.; Babizhetskyy, V.; Chykhriy, S.; Aksel'rud, L.; Stoyko, S.; Bauer, J.; Guérin, R.; Kuz'ma, Y. *Inorg. Mater.* 2004, **40**, 380.
- [24] Hill, R. J.; Howard, C. J. *J. Appl. Cryst.* 1987, **20**, 467.
- [25] Bish, D. L.; Howard, S. A. *J. Appl. Cryst.* 1988, **21**, 86.
- [26] Berrada, A.; Lapierre, M. F.; Loegel, B.; Panissod, P.; Robert, C. A. *J. Phys. F: Metal. Phys.* 1978, **8**, 845.
- [27] Tsaia, Y. Y.; Wub, F. B.; Chena, Y.; Penga, P. J.; Duhb, J. G. *Surf. Coat. Tech.* 2001, **146-147**, 502.
- [28] Bai, A.; Chuang, P. Y.; Hu, C. C. *Mater. Chem. Phys.* 2003, **82**, 93.
- [29] Hu, C. C.; Bai, A. *Surf. Coat. Tech.* 2001, **137**, 181.
- [30] Zhang, B. W.; Hu, W. Y.; Zhang, Q. L.; Qu, X. Y. *Mater. Character.* 1996, **32**, 119.
- [31] Yamamoto, T. *X-Ray Spectrom.* 2008, **37**, 57.
- [32] Waychunas, G. A.; Apted, M. J.; Brown, G. E. *Phys. Chem. Minerals.* 1983, **10**, 1.
- [33] Waychunas, G. A.; Brown, G. E.; Apted, M. J. *Phys. Chem. Minerals.* 1986, **13**, 31.
- [34] Wilke, M.; Farges, F.; Petit, P. E.; Brown, G. E.; Martin, F. *Am. Mineral.* 2001, **86**, 714.
- [35] Farges, F. C.; Brown, G. E.; Petit, P. E.; Munoz, M. *Geochim. Cosmochim. Acta.* 2001, **65**, 1665.
- [36] Hatsui, T.; Takata, Y.; Kosugi, N. *J. Synchrotron Rad.* 1999, **6**, 376.
- [37] Colpas, G. J.; Maroney, M. J.; Bagyinka, C.; Kumar, M.; Willis, W. S.; Suib, S. L.; Mascharak, P. K.; Baidya, N. *Inorg. Chem.* 1991, **30**, 920.
- [38] Marcus, M. A.; Flood, W.; Stiegerwald, M.; Brus, L.; Bawendi, M. *J. Phys. Chem.* 1991, **95**, 1572.
- [39] Lu, K. Q.; Wan, J. *Phys. Rev. B* 1987, **35**, 4497.
- [40] Franke, R.; Hormes, J. *Physica B.* 1995, **216**, 85.

- [41] Hesterberg, D.; Zhou, W. Q.; Hutchison, K. J.; Suzanne, A.; Sayers, D. E. *J. Synchrotron Rad.* 1999, **6**, 636.
- [42] Gassa, W.; Kruse, J. *Environ. Sci. Technol.* 2010, **44**, 2092.
- [43] Ingall, E. D.; Brandes, J. A.; Diaz, J. M.; Jonge, M. D.; Paterson, D.; McNulty, I.; Elliotte, W. C.; Northrup, P. *J. Synchrotron Rad.* 2011, **18**, 189.
- [44] Prietzel, J.; Dümig, A.; Wub, Y. H.; Zhou, J.; Klysubun, W. *Geochim. Cosmochim. Acta.* 2013, **108**, 154.
- [45] Franke R.; Hormes J. *Physica B* 1995, **216**, 85.
- [46] Anspoks, A.; Kuzmin, A. J. *Non-Cryst. Solids*, 2011, **357**, 2604.
- [47] Watanabe, T.; Kato, J.; Matsuo, S.; Wakita, H.; Umesaki, N. *X-Ray Spectrom* 2001, **30**, 15.
- [48] Hur, K. H.; Jeong, J. H.; Lee, D. N. *J. Mater. Sci.* 1991, **26**, 2037.

Captions for Figures

- Figure 1.** XRD patterns of Ni-P samples after heat-treatment at different temperatures.
- Figure 2.** (a) Typical refinement result of the XRD pattern for the Ni-P nanoparticles annealed at 700°C. The peaks ranging from 40 to 50° were enlarged in the inset for clarity. (b) Changes of phase contents with the heat-treatment temperature. These phase contents were obtained from the refinements of XRD patterns.
- Figure 3.** HRTEM image (a) and XRD pattern (b) of the as-prepared Ni-P nanoparticles before heat treatment. There is no observable long-range ordered clusters in the HRTEM image, indicating the amorphous attribute of the as-prepared Ni-P nanoparticles. Two very broad peaks around 45° and 83° confirm the amorphous nature of the as-prepared Ni-P nanoparticles.
- Figure 4.** HRTEM pictures of the Ni-P nanoparticles annealed at 550°C. The nanoparticles are encapsulated with a thin shell as shown in (a). The d-spacings of the crystalline nanoparticles are about 0.6 nm or 0.19 nm, some tiny metastable-phase crystallites can be observed coexisting with the amorphous phase in the enclosed shell, as shown in (b) and (c). The overlap of nanoparticles with different crystalline structures can be observed in (d). Two sets of diffraction patterns from Ni₃P and Ni confirm that the sample is a mixture phases as shown in (e).
- Figure 5.** HRTEM pictures of the Ni-P nanoparticles annealed at 750°C. The particle morphology shows that some nanoparticles tend to aggregate into bigger particles and there are some smaller particles around the bigger ones as shown in (a). The bigger and smaller particles are, respectively, well-crystallized into Ni₃P and Ni, and a pretty thin amorphous layer can still be observed to enclose the crystalline particles as shown in (b) and (c), without the remainder of the metastable phase. The SAED patterns of the these nanoparticles confirm the well-ordered single-crystal structures of Ni₃P

and FCC Ni nanoparticles.

Figure 6. (a) X-ray absorption spectra of the Ni-P nanoparticles with different heat-treatment temperatures. (b) k^3 -weight EXAFS functions of all the Ni-P nanoparticles. (c) Fourier transforms spectra of EXAFS signals for all the Ni-P nanoparticles. (d) A typical EXAFS fitting in R -space for the specimen heated at 750°C. (e) A typical EXAFS fitting in k -space for the specimen heated at 750°C.

Figure 7. Structure parameters extracted from the fitting results using theoretical Ni and Ni₃P crystalline structure models. (a) Variation of Ni-Ni coordination number with heat-treated temperature in FCC-Ni and TCP-Ni₃P crystallites. (b) Variation of Ni-P coordination number with heat-treated temperature in FCC-Ni and TCP-Ni₃P crystallites. (c) Variation of Ni-Ni bondlengths with heat-treated temperature in FCC-Ni and TCP-Ni₃P crystallites. (d) Variation of Ni-P bondlengths with heat-treated temperature in FCC-Ni and TCP-Ni₃P crystallites. (e) Stand Deviation of $\Delta R/R$ deviated from theoretical bondlengths. (f) Variation of Debye-Waller factors with heat-treatment temperature for the average Ni-Ni and Ni-P atom-pairs. Ni1, Ni2, and Ni3 represent the three inequivalent 8g sites occupied by Ni atoms in the TCP-Ni₃P crystal. Subscripts “E” and “T” represent, respectively, the experimental and theoretical values.

Figure 8. (a) P K-edge X-ray absorption spectra measured in fluorescence mode. (b) P K-edge k^3 -weight XAFS functions of the specimens at different heat-treatment temperatures. (c) Fourier transforms spectra of the P K-edge k^3 -weighted EXAFS functions. (d) A typical fitting curve of the EXAFS signal in R -space for the specimen heated at 750°C. (e) A typical fitting curve of the EXAFS signal in k -space for the specimen heated at 750 °C

Figure 9. Near-neighbor fitting Structure parameters of for the first P K-edge XAFS spectra for all the specimens with different heat-treatment temperatures. shell extracted from EXAFS fitting results. Theoretical value calculated from theory model Ni₃P were presented as dot line with in red color. (a) Average change of P-Ni shows variation of

coordination numbers with heat-treatment temperature. (a) Average change of Ni atoms centered around P atom, and (b) Average change of P-Ni bondlengths with heat-treatment temperature. and (c) Root-mean-square Standard deviation of $\Delta R/R$ of the fitting bondlength show the P-Ni bondlengths and their deviation from the theoretical values., respectively and correspondingly. Theoretical coordination number and bondlength from Ni_3P crystal are presented as the dot lines.

Figure 10. Magnetization vs. applied field hysteresis loops measured at room temperature. (a) M-H hysteresis loops for the samples annealed at different temperatures. (b) Saturated magnetic moment (M_s) of the samples annealed at different temperatures. It shows a sharp increase at first and then reach to a peak of 7.75 emu/g after the sample was heated to 750°C, presenting a positive correlation with the content of FCC-Ni phase. (c) Comparison of M-H hysteresis loops between Ni powders and the sample annealed at 750°C. Clearly, all the samples exhibit significantly decreased magnetization as compared with Ni powders, due to effect of phosphorus.

Figure 11. Crystallization behavior of Ni-P nanoparticles with high-P content (a) and low-P content (b). Three stages were used to clearly describe the crystallization of high-P amorphous Ni-P nanoparticles due to the appearance of metastable phase. The crystallization of low-P nanoparticles is relatively simple. The XRD-amorphous Ni-P nanoparticles with low-P content were directly transformed into Ni_3P and Ni crystalline phases.

Table of Contents entry

Crystallization process of noncrystalline Ni-P nanoparticles could be evaluated quantitatively through standard deviation of $\Delta R/R$ from XAFS spectra of P.

